

## The Impact of Moisture on Mountain Waves during T-REX

QINGFANG JIANG

*University Corporation for Atmospheric Research, Monterey, California*

JAMES D. DOYLE

*Naval Research Laboratory, Monterey, California*

(Manuscript received 3 March 2009, in final form 27 May 2009)

### ABSTRACT

The impact of moist processes on mountain waves over Sierra Nevada Mountain Range is investigated in this study. Aircraft measurements over Owens Valley obtained during the Terrain-induced Rotor Experiment (T-REX) indicate that mountain waves were generally weaker when the relative humidity maximum near the mountaintop level was above 70%. Four moist cases with a RH maximum near the mountaintop level greater than 90% have been further examined using a mesoscale model and a linear wave model. Two competing mechanisms governing the influence of moisture on mountain waves have been identified. The first mechanism involves low-level moisture that enhances flow–terrain interaction by reducing windward flow blocking. In the second mechanism, the moist airflow tends to damp mountain waves through destratifying the airflow and reducing the buoyancy frequency. The second mechanism dominates in the presence of a deep moist layer in the lower to middle troposphere, and the wave amplitude is significantly reduced associated with a smaller moist buoyancy frequency. With a shallow moist layer and strong low-level flow, the two mechanisms can become comparable in magnitude and largely offset each other.

### 1. Introduction

Moist processes have been largely ignored in the majority of mountain-wave studies, partially because of the complexity associated with moisture and microphysical processes. Studies of the interaction between moist airflow and mesoscale topography can be broadly classified into two categories. The first category includes quasi-analytical studies with highly simplified representations of moist processes. For example, a set of two-dimensional steady-state linear wave solutions including moist processes such as upslope condensation, leeside evaporation, and upslope precipitation were provided by Smith and Lin (1982). In their study, the latent heat warming or cooling associated with moist processes was represented by a variety of analytical heating functions. It has been demonstrated by Barcilon et al. (1979) that, in the presence of reversible moist processes, the dry linear wave equation is still valid after replacing the dry buoyancy

frequency ( $N$ ) with a moist buoyancy frequency ( $N_w$ ). Therefore, if the moist buoyancy frequency is known a priori, the moist wave solution can be derived without explicitly considering latent heating and cooling processes. The analytical studies by Barcilon et al. (1979, 1980) and the steady-state nonlinear solutions presented in Barcilon and Fitzjarrald (1985) indicate that moisture can play a dual role in modifying mountain waves and wave drag. A moist layer that is adjacent to the topography tends to weaken mountain waves and reduce wave drag and, on the other hand, a moist layer aloft could enhance waves and increase wave drag. In addition, the wave characteristics may be affected by precipitation as well (Barcilon et al. 1980). In fact, the moist processes associated with precipitation are irreversible, and consequently, the moist  $N$  approach is not strictly applicable to moist mountain waves in the presence of heavy precipitation.

The second category of studies of moist airflow interaction with topography includes numerical studies using mesoscale models with explicit cloud parameterizations. The impact of moisture on trapped waves has been examined by Durran and Klemp (1982a) using a nonlinear

---

Corresponding author address: Qingfang Jiang, Naval Research Laboratory, 7 Grace Hopper Ave., Monterey, CA 93940-5502.  
E-mail: jiang@nrlmry.navy.mil

Report Documentation Page			Form Approved OMB No. 0704-0188		
Public reporting burden for the collection of information is estimated to average 1 hour per response, including the time for reviewing instructions, searching existing data sources, gathering and maintaining the data needed, and completing and reviewing the collection of information. Send comments regarding this burden estimate or any other aspect of this collection of information, including suggestions for reducing this burden, to Washington Headquarters Services, Directorate for Information Operations and Reports, 1215 Jefferson Davis Highway, Suite 1204, Arlington VA 22202-4302. Respondents should be aware that notwithstanding any other provision of law, no person shall be subject to a penalty for failing to comply with a collection of information if it does not display a currently valid OMB control number.					
1. REPORT DATE <b>2009</b>	2. REPORT TYPE		3. DATES COVERED <b>00-00-2009 to 00-00-2009</b>		
4. TITLE AND SUBTITLE <b>The Impact of Moisture on Mountain Waves During T-REX</b>			5a. CONTRACT NUMBER		
			5b. GRANT NUMBER		
			5c. PROGRAM ELEMENT NUMBER		
6. AUTHOR(S)			5d. PROJECT NUMBER		
			5e. TASK NUMBER		
			5f. WORK UNIT NUMBER		
7. PERFORMING ORGANIZATION NAME(S) AND ADDRESS(ES) <b>University Corporation for Atmospheric Research, Monterey, CA</b>			8. PERFORMING ORGANIZATION REPORT NUMBER		
9. SPONSORING/MONITORING AGENCY NAME(S) AND ADDRESS(ES)			10. SPONSOR/MONITOR'S ACRONYM(S)		
			11. SPONSOR/MONITOR'S REPORT NUMBER(S)		
12. DISTRIBUTION/AVAILABILITY STATEMENT <b>Approved for public release; distribution unlimited</b>					
13. SUPPLEMENTARY NOTES					
14. ABSTRACT					
15. SUBJECT TERMS					
16. SECURITY CLASSIFICATION OF:			17. LIMITATION OF ABSTRACT <b>Same as Report (SAR)</b>	18. NUMBER OF PAGES <b>19</b>	19a. NAME OF RESPONSIBLE PERSON
a. REPORT <b>unclassified</b>	b. ABSTRACT <b>unclassified</b>	c. THIS PAGE <b>unclassified</b>			

numerical model with simple cloud physics. They demonstrated that moist processes in general weaken, and sometimes even disrupt trapped waves. Durran and Klemp (1983) studied the sensitivity of two-dimensional hydrostatic mountain waves to moist effects and concluded that moist processes tend to weaken hydrostatic waves as well. The interaction between the moist airflow and an isolated mountain have been investigated by Miglietta and Buzzi (2001) and Jiang (2003) using mesoscale numerical models. They found that low-level moisture could help airflow ascend over high topography and substantially reduce the upslope flow blocking. Doyle and Smith (2003) examined the latent heat effect on large-amplitude trapped waves in the Alps observed during the Mesoscale Alpine Programme and found that the latent heat release in the midtroposphere associated with precipitation plays a crucial role in forcing the low-level flow into the downslope windstorm regime and provides a pathway to the foehn. The interaction between a two-dimensional ridge and a nearly neutral moist airflow was recently studied by Miglietta and Rotunno (2005) and they found that the saturated airflow over the upwind slope can transition to unsaturated in the lee associated with strong descent.

Terrain blocking of moist airflow and its impact on orographic precipitation have been discussed in a number of model-based idealized and case studies (Buzzi et al. 1998; Colle 2004; Cox et al. 2005; Colle et al. 2008). Low-level flow blocking occurs frequently over the upwind slopes of major barriers such as the Sierra Mountains and European Alps, which has significant implications for mountain waves. For uniformly stratified hydrostatic flow past a two-dimensional ridge or an isolated hill, it has been demonstrated that the flow deceleration over the upwind slope is controlled by the nondimensional mountain height,  $M = N h_m / U_c$ , where  $h_m$  is the terrain height and  $U_c$  is the ambient cross-barrier wind component (Smith 1989; Smith and Grønås 1993). When the nondimensional mountain height exceeds a certain threshold (hereafter referred to the critical mountain height), the cross-barrier wind component can be reduced to zero over the upwind slope (referred to as flow stagnation), which implies severe low-level blocking. The critical nondimensional mountain height  $M_c$  for the onset of the upslope flow stagnation varies with the terrain horizontal aspect ratio (Smith 1989). Huppert and Miles (1969) found, in their modeling study, that  $M_c \approx 0.85$  for flow past a two-dimensional ridge. Based on a series of numerical simulations of nearly saturated stratified flows past a three-dimensional Gaussian hill, Jiang (2003) has demonstrated that the upslope flow deceleration and the onset of upwind flow stagnation can be predicted using a moist nondimensional mountain height,

$M_w = N_w h_m / U_c$ , where  $N_w$  is the average moist buoyancy frequency below the mountaintop level. Smith et al. (2002) suggested that in the presence of severe blocking, only the upper portion of mountains that is above the blocked layer contributes to mountain-wave generation. Based on this argument, an effective terrain height can be defined as  $h_{\text{eff}} = h - h_{\text{cutoff}}$ , where  $h$  is the real terrain height and  $h_{\text{cutoff}}$ , referred to as the cutoff mountain height in Smith et al. (2002), is the depth of the blocked layer. According to linear wave theory, the mountain-wave amplitude is proportional to the terrain height, and therefore, flow blocking in general weakens waves by reducing the effective terrain height.

It is noteworthy that most of the moist studies cited above are analytical or idealized studies of interaction between a steady moist airflow characterized by simple velocity, stratification, and moisture profiles and idealized topography, such as a two-dimensional ridge or an isolated hill. Observation-based studies of realistic synoptic flow past complex terrain are still rare. This study is inspired by observations obtained during the Terrain-induced Rotor Experiment (T-REX; Grubišić et al. 2008). Our primary objective is to examine the impact of moisture on mountain waves associated with the interaction between westerly or southwesterly moist airflow and the Sierra Mountains. T-REX took place over the Sierra Mountains and Owens Valley in March and April of 2006, and the objective was to enhance our understanding of mountain waves and wave-induced rotor circulations in the lee of the Sierra Nevada Range.

The remainder of the paper is organized as follows. Observational results are presented in section 2. The numerical model configuration is described in section 3. In section 4, diagnosis of four moist simulations is presented. The effects of moisture on low-level flow blocking and wave characteristics aloft are further examined in section 5. The results and conclusions are summarized in section 6.

## 2. Observational summary

### *a. Dependence of mountain waves on mountaintop winds and moisture*

The T-REX region of enhanced observations includes two nearly parallel mountain ranges, the Sierra Nevada and Inyo Mountains, with the quasi-two-dimensional Owens Valley located between the two ranges (Fig. 1). A variety of ground-based instruments, including automatic weather stations, flux towers, wind profilers, and scanning aerosol and Doppler lidars were deployed in Owens Valley near Independence, California. In addition, the University of Wyoming King Air (UWKA)

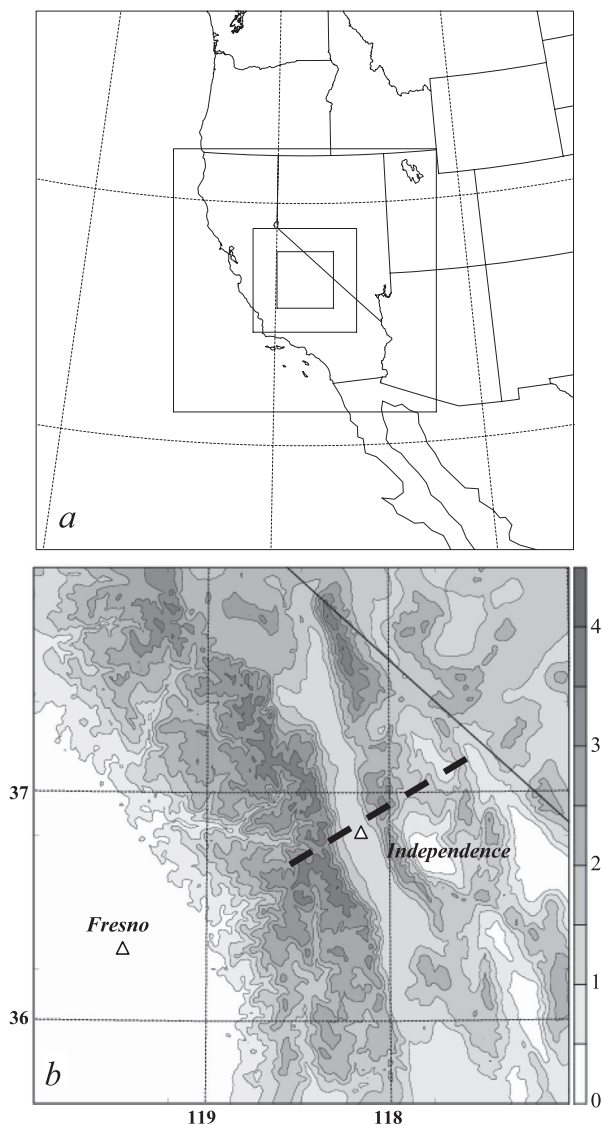


FIG. 1. (a) The four-level nested model grids and (b) the topography in the 1-km grid (grayscale and contours, interval: 0.5 km). The locations of Fresno and Independence are indicated by triangles. The UWKA flight track over Independence is shown as a dashed line in (b).

flew vertical stacks across Owens Valley, oriented approximately along the mountaintop wind direction (see Fig. 1), to sample gravity waves in the lower to middle troposphere (up to  $\sim 8$  km MSL). Twenty-four UWKA flights have been conducted to observe mountain waves associated with the westerly or southwesterly winds at the mountaintop level during the 2-month-long field campaign. During each Intensive Observational Period (IOP), GPS radiosondes have been launched from the upwind side of the Sierra Mountains [i.e., either from Lemoore, California, or the National Center for Atmospheric Research (NCAR) Mobile GPS Advanced

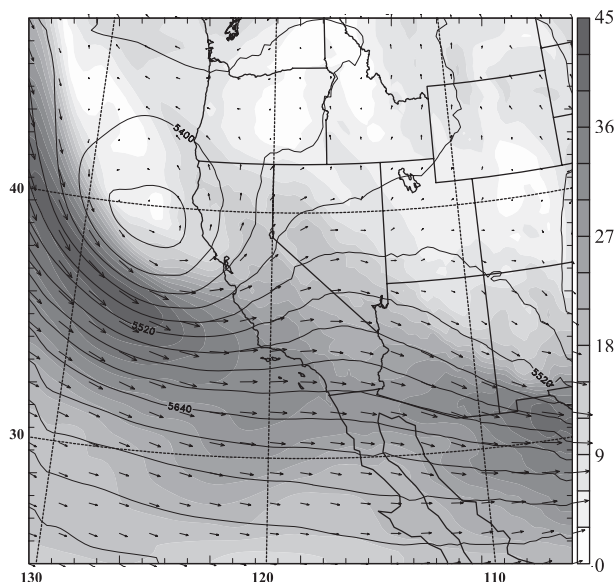


FIG. 2. The wind speed (grayscale, increment:  $3 \text{ m s}^{-1}$ ), wind vectors, and geopotential height contours (increment: 30 gpm) at 500 hPa derived from COAMPS 27-km grid, valid at 1800 UTC 20 Mar 2006.

Upper Air System (MGAUS) near Fresno, California; Fig. 1]. The large-scale flow conditions for a typical westerly T-REX IOP are shown in Fig. 2. A shortwave trough is positioned offshore of northern California, which directs strong westerly or southwesterly flow toward Owens Valley. The prevailing wind direction near the mountaintop level ( $\sim 4$  km MSL) during westerly IOPs is approximately perpendicular to the main Sierra ridge, which favors the generation of strong mountain waves over Owens Valley.

The relationship between the wave amplitudes, derived from UWKA measurements, and the cross-barrier wind component (i.e.,  $245^\circ$  from north) at the mountaintop level, derived from the upstream soundings is shown in Fig. 3a. Here the wave amplitude is defined as the maximum vertical velocity range along each wave traverse. Wave traverses refer to those flight segments that are characterized by smooth waves above the mountaintop. A radiosonde was launched from the upwind side of the Sierra Mountains every 3 h during each IOP. We assume that it takes about 3 h for airflow to travel the distance between the upstream sounding site at Fresno and Independence in Owens Valley, which is approximately 100 km. The upstream radiosonde with its launching time closest to  $t - 3$ , where  $t$  is the hour when the maximum wave amplitude was observed, is selected to represent the ambient flow condition.

In general, the measured wave amplitude tends to increase linearly with the cross-barrier wind component

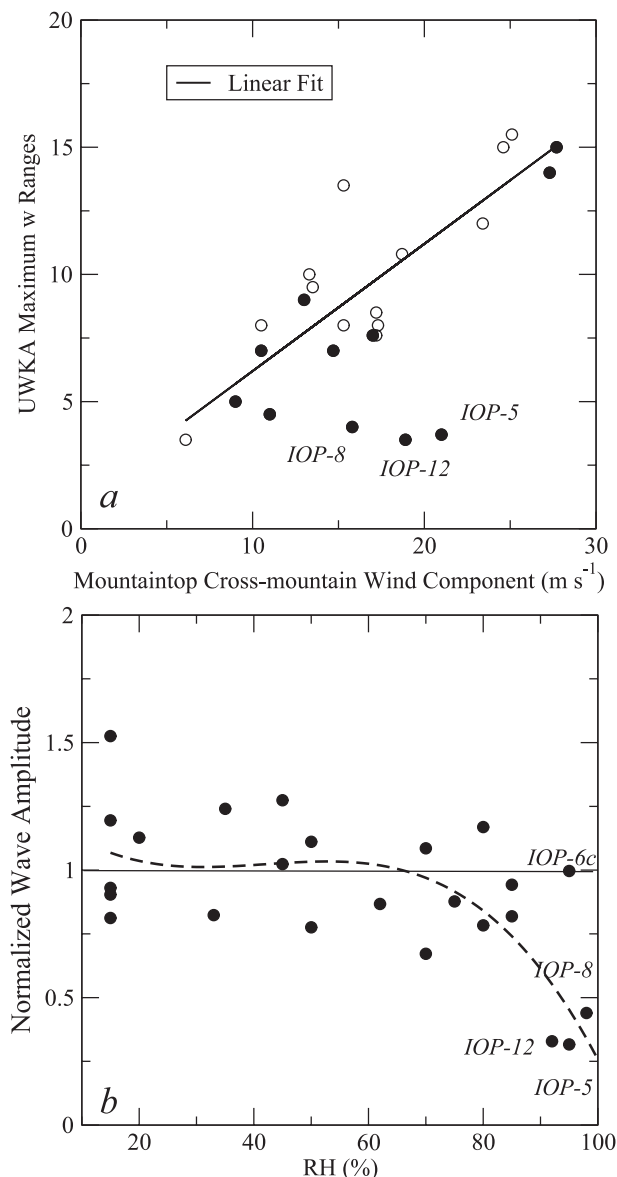


FIG. 3. (a) The scatterplot of UWKA observed wave amplitude vs the cross-barrier wind component at the mountaintop level derived from the upwind sondes for 24 UWKA flights. The filled circles represent moist cases as defined in the text. The bold line corresponds to the least squares regression line. (b) The normalized wave amplitude is plotted vs the upwind RH maximum. Points corresponding to the four very moist cases are labeled. The dashed curve represents a third-order polynomial regression using all the data points except for IOP-6c.

at the mountaintop level (Fig. 3a). It is noteworthy that the wave amplitudes from the flights of IOP-5, IOP-8, and IOP-12 are well below the average trend and show little sensitivity to the upstream wind speed. After removing these three outliers, the linear least squares regression using the other 21 points yields

$$W(U_c) = 0.80 + 0.50U_c. \quad (1)$$

We refer to the wave amplitude,  $W(U_c)$ , given by (1) as the reference wave amplitude for a given upstream cross-barrier wind component,  $U_c$ . To examine the connection between the relative humidity (RH) and the Sierra wave amplitude, the cases with the relative humidity (i.e., with respect to water throughout this paper) maximum ( $RH_{\max}$ ) within a vertical distance of 1 km from the mountaintop level (i.e., 3–5 km MSL) greater than 70% are referred to as moist cases and shown as filled circles in Fig. 3a. According to this definition, there are 11 moist cases, approximately 46% of the events documented. It is evident that the wave amplitudes of most moist cases are smaller than their corresponding reference wave amplitudes. The wave amplitudes for the 24 flights normalized by the reference wave amplitude are plotted versus the upstream RH maxima in Fig. 3b. There are four very moist cases with  $RH_{\max} > 90\%$ , corresponding to IOP-5, IOP-6c (i.e., the third flight during IOP-6), IOP-8, and IOP-12, respectively. For three of the four very moist cases, namely, IOP-5, IOP-8, and IOP-12, which correspond to the three outliers in Fig. 3a, the observed wave amplitudes are only approximately one-third of the corresponding reference wave amplitudes. The dashed curve in Fig. 3b represents a third-order polynomial regression using all the data points except for IOP-6c. Despite the scatter, it is evident that for the relatively dry cases (i.e.,  $RH_{\max} < 70\%$ ) the mean normalized wave amplitude is close to unity and, for moist cases, the normalized wave amplitude tends to decrease with increasing RH, implying a strong influence of moisture on mountain waves. The normalized wave amplitude of IOP-6c is close to unity, although the upstream  $RH_{\max}$  for IOP-6c is above 90%.

It is noteworthy that the mountain waves observed during moist IOPs were much less steady than observed during dry IOPs. The time scale for mountain waves to establish in the troposphere is  $T \sim O(L/U_c)$ , where  $L$  is the mountain width and  $U_c$  is the characteristic cross-mountain wind component. Using  $L \sim 100$  km for the main Sierra ridge and  $U_c \sim 10$  m s<sup>-1</sup>, we obtain  $T \sim 3$  h, which is far shorter than typical synoptic time scales ( $\sim$  a few days). Therefore, we expect the tropospheric waves over the mesoscale terrain to be relatively steady. This has been confirmed by recent aircraft observations of mountain waves in the troposphere and lower stratosphere over the Alps (Smith et al. 2002) and the Sierra Mountains (Smith et al. 2008) for relatively dry wave events. The wave patterns observed within a vertical cross section during some T-REX moist IOPs were much less coherent, indicative of unsteadiness. The rapid evolution



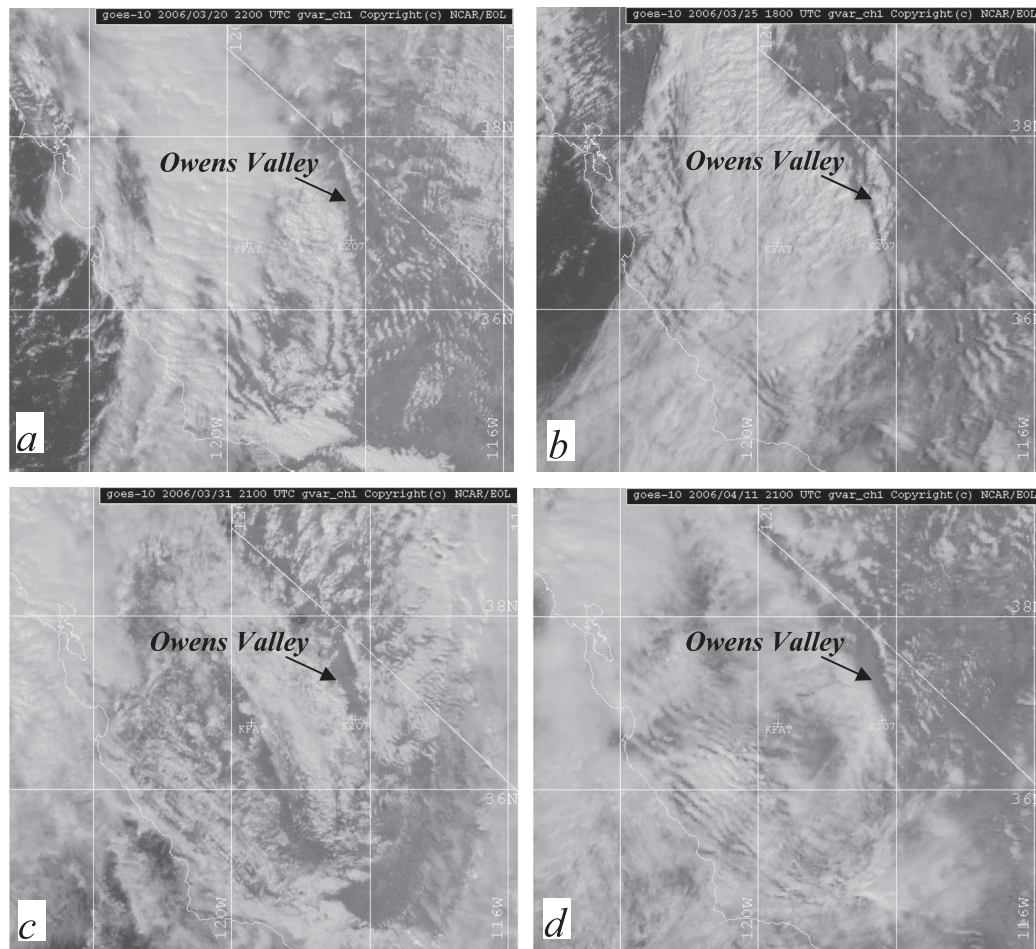


FIG. 4. GOES images valid at (a) 2200 UTC 20 Mar, (b) 1800 UTC 25 Mar, (c) 2100 UTC 31 Mar, and (d) 2100 UTC 11 Apr 2006.

or unsteadiness of the moist mountain waves is likely caused by fast temporal variation of the moisture content in the incoming flow and rapid microphysical processes with time scales typically less than 3 h. The 3-hourly radiosonde observations indicate substantial variations of water vapor content in the lower troposphere during the observational periods.

#### *b. The four moist IOPs*

The remainder of this paper focuses on the four very moist cases with the upstream  $RH_{\max} > 90\%$ . They correspond to the afternoon flight on 20 March (i.e., IOP-5), the afternoon flight on 25 March (IOP-6c), the afternoon flight on 31 March (IOP-8), and the morning flight on 11 April 2006 (IOP-12). The large-scale flow conditions are quite similar for these cases, characterized by a shortwave trough located off the California and Oregon coast (Fig. 2). The prevailing mountaintop winds are southwesterly and widespread low-level clouds are

evident around the observation periods (Fig. 4). In general, more clouds are present over the upwind side of the Sierra ridge. Upstream clouds are especially apparent IOP-6c; it was largely cloud free to the east of the Sierra Mountains, consistent with strong leeside descent. Foehn clearing over Owens Valley is evident for IOP-5, -6c, and -12, indicative of flow descent over the leeslope of the Sierra Mountains. The Geostationary Operational Environmental Satellite (GOES) image for IOP-8 shows widespread convective clouds and a thin line of clearing over Owens Valley, suggestive of relatively weak leeside descent.

The profiles of cross-barrier winds, potential temperature, and relative humidity from four upstream radiosondes corresponding to the flight periods of the four cases are shown in Fig. 5. At the mountaintop level ( $\sim 4$  km MSL), IOP-6c has the strongest cross-barrier wind speed ( $\sim 27 \text{ m s}^{-1}$ ) and IOP-8 has the weakest wind speed ( $\sim 16 \text{ m s}^{-1}$ ). Below the mountaintop, the

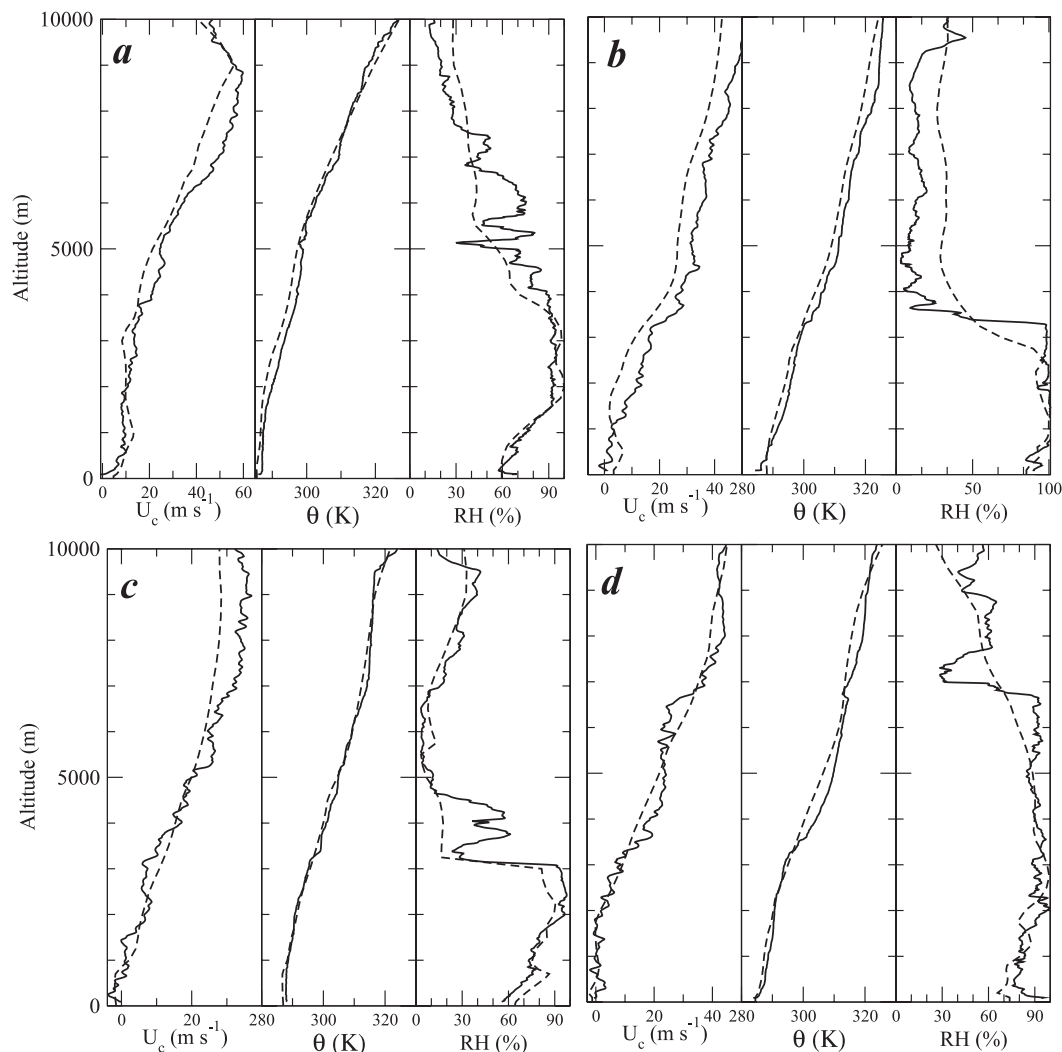


FIG. 5. Profiles of the cross-barrier wind component ( $\text{m s}^{-1}$ ), potential temperature ( $\theta$ , K), and relative humidity (with respect to water, %) for (a) IOP-5, (b) IOP-6c, (c) IOP-8, and (d) IOP-12. The solid and dashed curves correspond to the profiles derived from the upstream soundings and the COAMPS simulated profiles at the same location and approximately same times.

mean cross-barrier winds are weak for IOP-8 and -12 and much stronger for IOP-5 and -6c. The potential temperature profiles indicate that the incoming airflow is generally less stable below 2 km MSL and more stable above the mountaintop level. It is noteworthy that for all four soundings, the Scorer parameter,  $l^2 = N^2/U_c^2 - U_{cz}/U_c$ , decreases with altitude above the mountaintop level, associated with the forward shear in the  $U_c$  profiles. It is well established that a decrease of the Scorer parameter with height favors the formation of trapped waves (Scorer 1949). The RH profiles indicate that a deep moist layer up to 7 km is present in IOP-5 and -12. The moist layer is much shallower ( $\sim 3\text{--}4$  km MSL) for IOP-6c and -8 (Table 2).

### 3. Model description

The atmospheric component of the Coupled Ocean–Atmosphere Mesoscale Prediction System (COAMPS,<sup>1</sup> Hodur 1997) is used for this study. COAMPS is a nonlinear, compressible, nonhydrostatic terrain-following mesoscale model with a suite of physical parameterizations. The turbulent mixing and diffusion are represented using a prognostic equation for the turbulence kinetic energy (TKE) budget (Mellor and Yamada 1974). The surface heat and momentum fluxes are computed

<sup>1</sup> COAMPS is a registered trademark of the Naval Research Laboratory.

following the Louis (1979) and Louis et al. (1982) formulation. The grid-scale evolution of the microphysical processes is explicitly predicted from budget equations for cloud water, cloud ice, rainwater, snow water, and water vapor mixing ratios (Rutledge and Hobbs 1983) and the subgrid-scale moist convective processes are parameterized using an approach following Kain and Fritsch (1993). The short- and longwave radiation processes are parameterized following Harshvardhan et al. (1987).

The initial fields for the model are created from multivariate optimum interpolation analysis of upper-air sounding, surface, commercial aircraft, and satellite data that are quality controlled and blended with the 12-h COAMPS forecast fields. Lateral boundary conditions for the outermost grid mesh are derived from Navy Operational Global Analysis and Prediction System (NOGAPS) forecast fields. The computational domain contains four horizontally nested grid meshes (i.e., one-way nesting) of  $91 \times 91$ ,  $131 \times 131$ ,  $157 \times 157$ , and  $256 \times 256$  grid points, and the corresponding horizontal grid spacings are 27, 9, 3, and 1 km, respectively. There are 60 levels in the vertical on a nonuniform sigma grid with finer spacings in the lower troposphere. The model top is located approximately at 30 km MSL and a sponge boundary condition is applied to the upper one-third of the domain to reduce the downward reflection of gravity waves (Klemp and Lilly 1978). The terrain data is based on the Global Land One-km Base Elevation (GLOBE) dataset. The 1-km mesh is centered at Independence and the terrain in the 1-km mesh is shown Fig. 1b.

For the four moist cases examined in this study, the model is initialized at 1200 UTC 20 March, 25 March, 31 March, and 11 April 2006, respectively, and integrated over 18 h. The first 4 h of each simulation is considered to be the spinup period and only the output data from the 4–18-h period are used for diagnosis. For each case, a pair of simulations have been performed. The simulation with full physics is referred to as the control simulation. In addition to the control simulation, a sensitivity simulation is carried out for each case with the identical model configuration except that microphysical processes such as condensation, evaporation, ice physics, and precipitation are turned off in the 1-km grid, which is referred to as the dry simulation. It is noteworthy that the simulations in the 27-, 9-, and 3-km grids are identical for each pair of simulations to ensure that the large-scale flow conditions are comparable for each pair of control and dry simulations. For the convenience of description, the control and dry simulations are referred to as CTRLX and DRYX, where X = 5, 6c, 8, and 12, corresponding to IOP-5, -6c, -8, and -12, respectively.

TABLE 1. Comparison of wave characteristics between the UWKA observed (obs) and COAMPS simulated (CTRL) primary lee waves over Owens Valley within the UWKA flight cross section.

IOP	Wave type (obs/CTRL)	Wavelength (km)		Maximum-wave range ( $\text{m s}^{-1}$ )	
		(obs/CTRL)		(obs/CTRL)	
5	Trapped/trapped	9/9.5		3.5/4.2	
6c	Hydrostatic/hydrostatic	28/30		15.0/16.5	
8	Trapped/trapped	10/11		3.8/4.1	
12	Trapped/trapped	9/9.5		3.2/4.9	

For the four moist cases, the simulated wind, potential temperature, and RH profiles are included in Fig. 5 for comparison with the radiosonde observations. The profiles are derived from the control simulations. There are some noticeable discrepancies between the modeled and observed profiles. For example, the simulated cross-barrier wind component from CTRL6c is weaker than the observed in the troposphere. Overall, the agreement between the control simulations and observations is encouraging. In particular, COAMPS reasonably captures the relatively deep moist layers in IOP-5 and -12 and shallower moist layers in IOP-6c and -8. The simulated wind speed increases with altitude between the mountaintop level and the tropopause, which is in agreement with the radiosonde observations. The satisfactory agreement between the control simulations and the radiosonde observations suggests that general characteristics of the large-scale flows for the four moist cases are well simulated.

The unsteadiness of the Sierra waves during the four moist IOPs makes any direct comparison between the UWKA in situ measurements and the control simulations difficult. A crude comparison is given in Table 1, where some characteristics of the primary lee waves over Owens Valley along the UWKA flight cross section derived from the UWKA observations and COAMPS control simulations are listed. It is evident that the COAMPS-simulated wave characteristics and wavelengths are in good agreement with the observations. However, the simulated waves are in general somewhat stronger than observed.

#### 4. Numerical results

In this section, the characteristics of the simulated mountain waves derived from the control and the corresponding dry simulations of each moist case are illustrated. The objectives are threefold: (i) to understand the impact of moisture on wave characteristics such as wave amplitude and wave momentum fluxes, (ii) to examine the role of low-level moisture in low-level flow



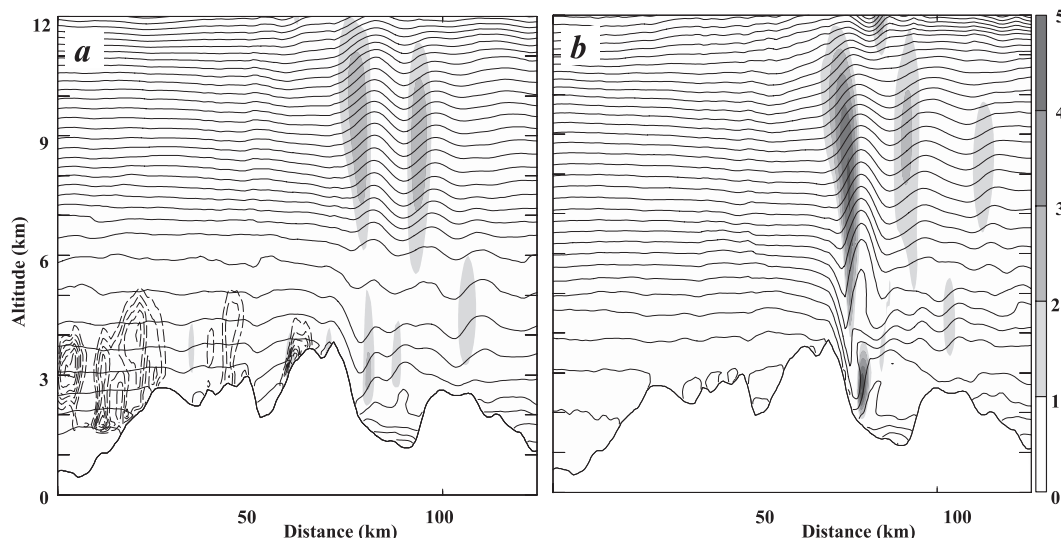


FIG. 6. Vertical cross sections of updraft (grayscale, increment:  $1 \text{ m s}^{-1}$ ), potential temperature (solid contours, increment:  $1 \text{ K}$ ), total cloud water mixing ratio (dashed contours, increment:  $0.05 \text{ g kg}^{-1}$ ) valid at 0000 UTC 21 Mar 2006 derived from IOP-5 simulations. The cross section is oriented across valley approximately along the UWKA flight track shown in Fig. 1. (a) Control and (b) dry simulations.

blocking, and (iii) to evaluate the influence of the moist layer on the wave amplitude aloft.

#### a. The impact of moisture on wave characteristics

We start by examining vertical cross sections derived from the control and dry simulations for each case. These cross sections are oriented along the UWKA flight track (Fig. 1b) and are valid approximately at the corresponding observational times.

For IOP-5, two trapped wave modes are present in the lee of the Sierra ridge in the control simulation (Fig. 6a): one is located in the lower troposphere with a horizontal wavelength of approximately 9 km and the other is centered in the upper troposphere with a longer horizontal wavelength ( $\sim 18 \text{ km}$ ). Trapped waves are determined here by the following criteria: (i) the phase lines are vertically oriented and (ii) the wavenumber is larger than the smallest Scorer parameter in the layer above the wave. A wave becomes evanescent (or trapped) when it propagates into a layer with Scorer parameter less than the horizontal wavenumber (Scorer 1949). The upper trapped wave mode appears in the corresponding dry simulation as well. However, compared to the control simulation, the wave amplitude in the dry simulation is more than doubled and the vertical wavelength is noticeably shorter. In the lower troposphere, a hydraulic-jump-like structure, characterized by sharp ascent and nearly vertical isentropes (Fig. 6b), is evident in DRY5, and the updraft associated with the jump is significantly stronger than that induced by the short trapped wave in CTRL5.

IOP-6c is characterized by a deep hydrostatic wave extending from the valley floor up to the tropopause (Fig. 7a). The wave amplitude and the horizontal wavelength ( $\sim 30 \text{ km}$ ) are much larger than those of IOP-5. The upslope cloud top is approximately 1 km higher than the top of the moist layer observed upstream (Fig. 5b), indicative of strong upslope ascent. In the absence of moist processes, the wave amplitude becomes considerably larger (Fig. 7b), implying that moist processes tend to weaken waves for IOP-6c as well.

For both CTRL8 and DRY8, a small-amplitude trapped wave is located in the lee of the Sierra ridge, which decays rapidly downstream (Fig. 8). A thin layer of clouds is present over the upwind slope in CTRL8, consistent with the shallow moist layer shown in the RH profile for IOP-8 (Fig. 5c). Consequently, the wave characteristics shown in the corresponding dry simulation (Fig. 8b) are similar to those in the control simulation except that the wave amplitude is slightly smaller.

In CTRL12, a deep cloud layer is located over the upwind slope, which extends downstream over half of the valley (Fig. 9a). The cloud water mixing ratios are substantially smaller than in the CTRL6c section, indicating a much weaker upslope ascent associated with the weaker low-level cross-barrier winds (Fig. 5d). A trapped wave is evident over the lee slope of the Sierra ridge in CTRL12. Compared to the control simulation, the trapped wave in the corresponding dry simulation is much stronger and more wave energy leaks into the upper troposphere as well (Fig. 9b).

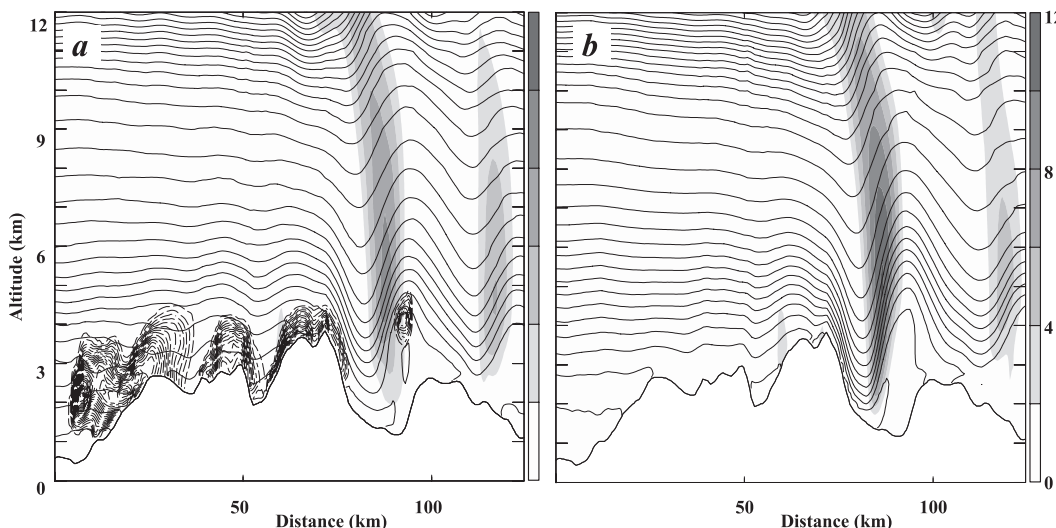


FIG. 7. As in Fig. 6, but for IOP 6c. The increment of updraft is  $2 \text{ m s}^{-1}$  and the increment of total cloud water mixing ratio is  $0.05 \text{ g kg}^{-1}$ .

In summary, by contrasting the cross sections from the control and dry simulations, we find that moist processes in general tend to weaken waves (IOP-5, -6c, and -12). Moisture could alter the wave modes (IOP-5) and the vertical wavelength (IOP-5) as well. The impact of moisture on waves appears to be dependent on the depth of the low-level moist layer and the cross-barrier winds below the mountaintop level.

*b. The impact of moisture on wave momentum fluxes*

The above discussion is largely based on diagnosis of the wave characteristics along a vertical cross section defined by the UWKA flight segment. To examine the

impact of moist processes using a domain-wide wave metric, we compute the domain-averaged vertical flux of the cross-barrier horizontal momentum component for each control-dry pair of simulations. The cross-barrier momentum flux is defined as

$$M_c(z, t) = \frac{\bar{\rho}(z) \int_A u'_c w' dx dy}{A}, \quad (2)$$

where  $u'_c = u_c - \bar{u}_c$  and  $w' = w - \bar{w}$  denote the cross-barrier wind and vertical velocity perturbations,  $\bar{\rho}(z)$  is the air density, the overbar denotes the domain-wide

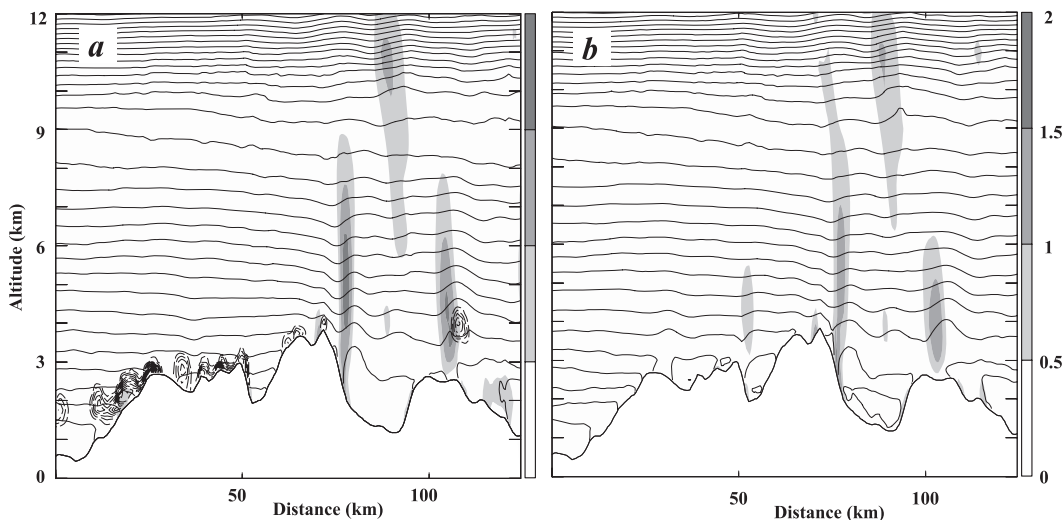


FIG. 8. As in Fig. 6, but for IOP 8 valid at 2100 UTC 31 Mar 2006 and the updraft increment is  $0.5 \text{ m s}^{-1}$ .

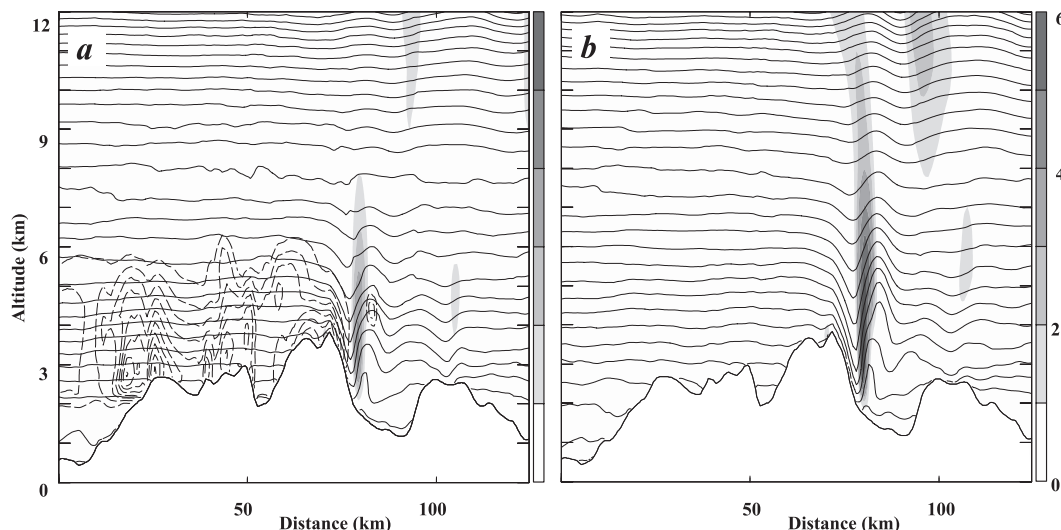


FIG. 9. As in Fig. 6, but for IOP 12.

ensemble average, and  $A$  is the domain area. The time–height diagrams of the cross-barrier wave momentum fluxes are shown in Fig. 10 for the control and dry simulations of IOP-5. It is evident that in the early hours of the simulation the momentum fluxes from the two simulations are comparable (Figs. 10a,b), likely due to the fact that the airflow is still relatively dry in the early hours of the simulation (Fig. 10c). The amplitude of the momentum flux from CTRL5 becomes significantly smaller than that of the DRY5 simulation associated with the arrival of the moist airflow, implying that the mountain waves have been substantially weakened by moist processes during IOP-5. For IOP-6c, the dry simulation produces stronger waves than the control simulation (Fig. 11). In contrast, for IOP-8 and IOP-12, the waves are much weaker and the differences in the momentum fluxes from the control and dry simulations are relatively small (not shown), suggesting that the impact of moisture on the domain-average wave characteristics is small for IOP-8 and IOP-12. This is likely due to the weaker low-level flow in these two IOPs, which leads to deeper upwind blocking. Consequently, orographic clouds are only present over high peaks where appreciable ascent exists. The upwind blocking will be further discussed in the following sections.

### c. Low-level flow blocking

The term “blocking” in this study refers to the deceleration of surface winds by the terrain-induced positive pressure perturbations over the upwind terrain slope. Blocking tends to weaken mountain waves through a reduction of the vertical velocity near the terrain surface. For flow over a two-dimensional ridge, the lower

boundary condition is given by  $w_s = U_s(\partial h/\partial x)$ . Here  $U_s$  and  $w_s$  are the horizontal and vertical velocities along the terrain surface and  $\partial h/\partial x$  is the terrain slope. Over high mountains, the cross-barrier wind component over the windward slope could be significantly reduced by low-level flow blocking, which results in weaker vertical motion near the terrain surface.

To understand the impact of moist processes on the upwind flow blocking, the average cross-barrier wind component and vertical velocity over each 100-m elevation interval in a box over the upwind slope of the Sierra ridge (Fig. 12) is calculated and shown in Fig. 13 as a function of the elevation. Around the observation time of IOP-5, the cross-barrier wind component along the upwind surface from the control simulation is substantially stronger than from the corresponding dry simulation for elevations above 1.5 km MSL, implying that low-level moisture plays a significant role in reducing the upwind flow blocking (Fig. 13a). Consequently, the upslope ascent in the control simulation is much stronger than in the dry simulation. It is noteworthy that the low-level flow is relatively dry in the early hours of the IOP-5 simulation, and accordingly, the difference between the cross-barrier winds over the upwind slope from the control and dry simulations is small (not shown). IOP6c is characterized by the strongest low-level cross-barrier winds in the four IOPs examined (Fig. 3), and accordingly, the surface cross-barrier winds are substantially stronger than the other three cases (Fig. 13b). Between 1.5 and 2.75 km MSL, the cross-barrier winds and the upslope ascent are considerably stronger in CTRL6c than in DRY6c, indicative of the strong moisture impact on the upslope ascent. Both IOP-8

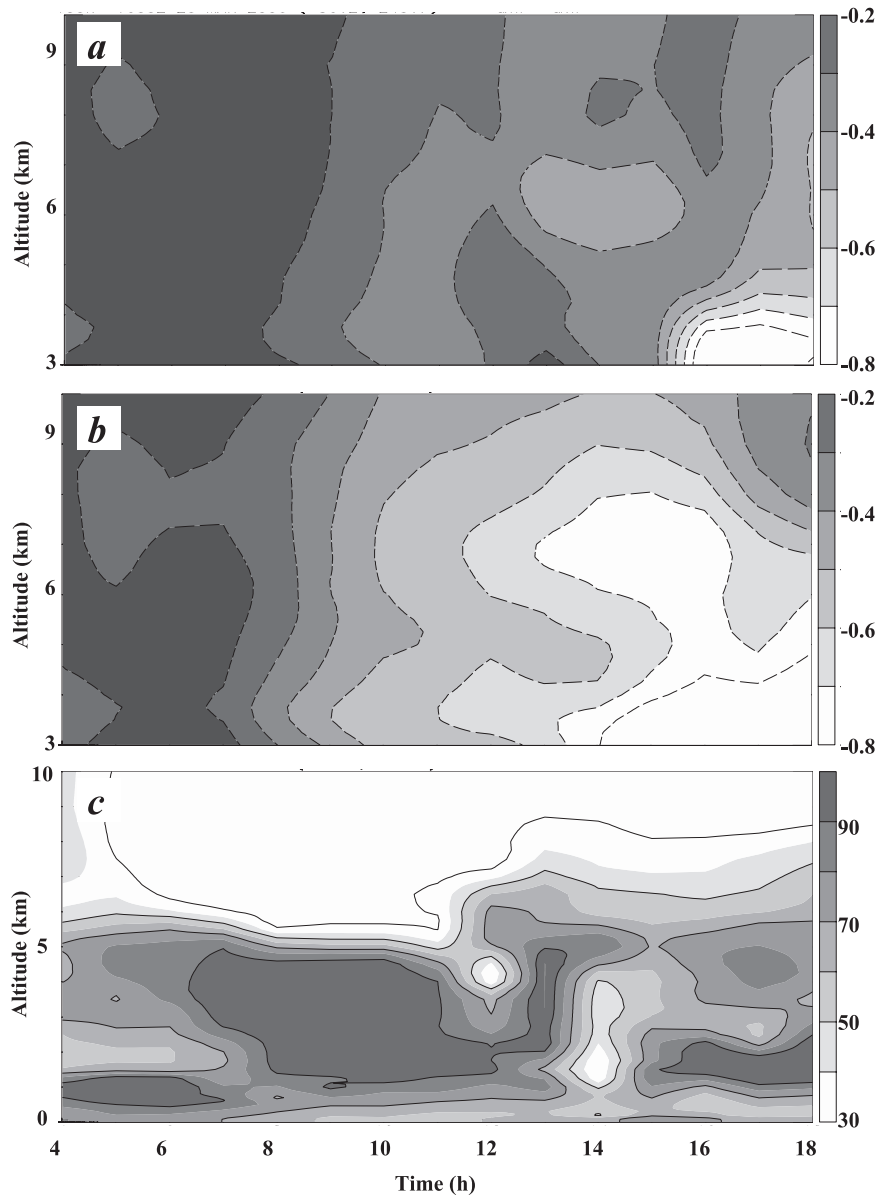


FIG. 10. (a),(b) The time–height sections of the vertical fluxes of the cross-valley momentum component (increment:  $0.1 \text{ N m}^{-2}$ ) computed from the control and dry simulations of IOP-5. (c) The time–height section of relative humidity (increment: 10%) at Fresno (see Fig. 1 for location). For the momentum fluxes in (a) and (b), only the portion between 3 and 10 km MSL is shown. The horizontal axis is in model time (h).

and IOP-12 are characterized by a deep blocked layer over the upwind slope (Figs. 13c,d), which is consistent with the weak low-level cross-barrier winds in the upstream wind profiles (Fig. 5). The cross-barrier winds and the upslope ascent are in general stronger in the control simulations than in the corresponding dry simulations of IOP-8 and -12, but compared to the IOPs with relatively strong low-level winds (i.e., IOP-5 and -6c), the difference between the dry and control simulations are much less pronounced.

The role of moisture in reducing blocking is explored further with a trajectory analysis. For each simulation, air parcels have been released at 1800 UTC from an upstream point (Fig. 12) and different altitudes. The forward trajectories are computed using  $\mathbf{x}_{n+1} = \mathbf{x}_n + \mathbf{V}(\mathbf{x}_n, t_n)\Delta t$ , where  $\mathbf{x}_n$  denotes the three-dimensional position vector at step  $n$ ,  $\mathbf{V}(\mathbf{x}_n)$  is the three-dimensional wind vector at position  $\mathbf{x}_n$ , and time  $t_n$  is linearly interpolated from the half-hour interval wind data from the

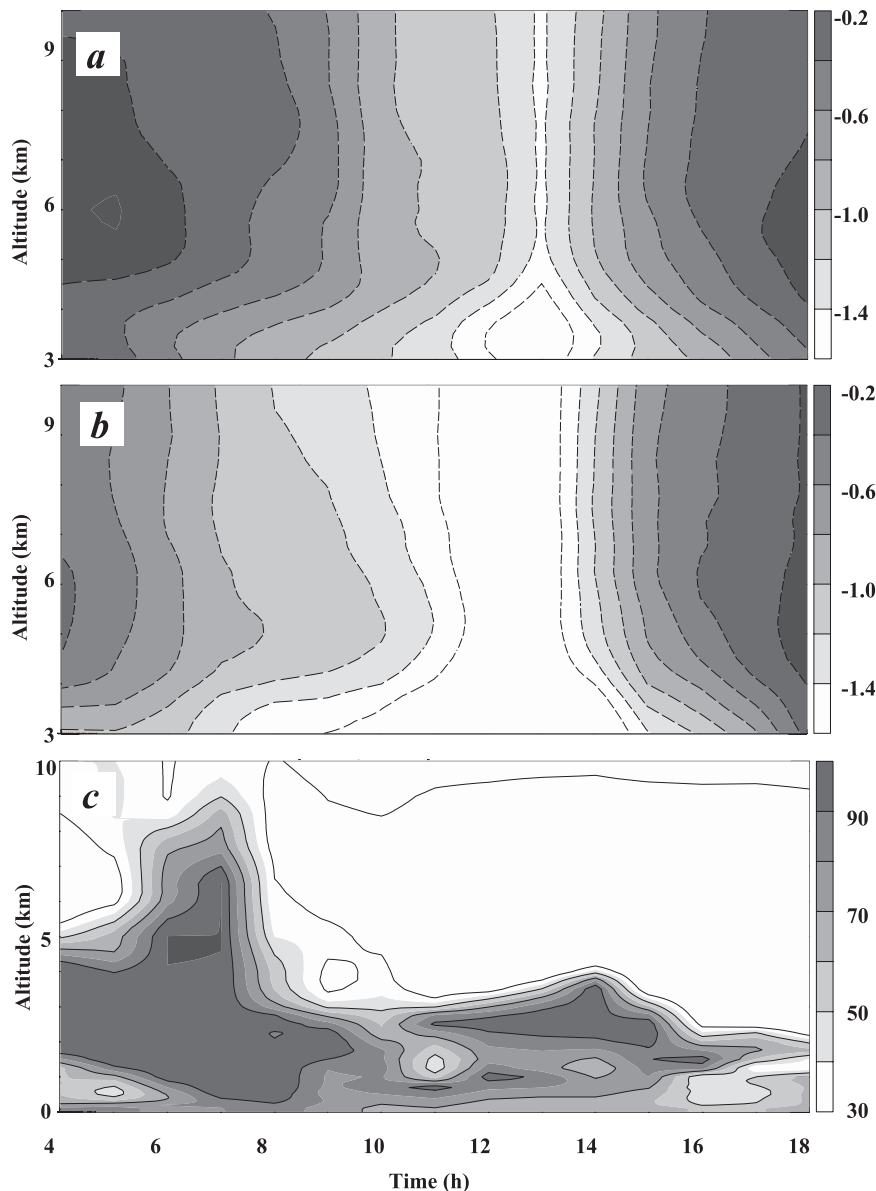


FIG. 11. (a),(b) As in Fig. 10, but for IOP-6 and the grayscale interval is  $0.2 \text{ N m}^{-2}$ .

COAMPS simulations. The time interval  $\Delta t$  is chosen to be 0.5 min for most calculations. In the absence of nonconservative processes such as radiation and mixing, the equivalent potential temperature of each Lagrangian air parcel should be conserved. For each trajectory calculation, the variation of the air parcel equivalent potential temperature has been checked to ensure the thermodynamic consistency. Trajectories with equivalent potential temperature (or potential temperature for dry simulations) change greater than 1 K are recalculated with a reduced time interval. As an example, some trajectories derived for the control and dry simulations of IOP-5 are shown in Fig. 12. It is evident that the

trajectories of parcels released from both 2.5 km and 3 km MSL are deflected more toward the north by the Sierra ridge in the dry simulation than in the corresponding control simulation. For example, an air parcel released from 2 km MSL is blocked to the windward side in the dry simulation and in contrast, ascends across the Sierra ridge in the control simulation. A similar trajectory analysis using winds from CTRL6c and CTRL12 indicates that, in the control simulations, the depth of the blocked layer upstream of Independence is significantly shallower than in their corresponding dry simulations, likely associated with moist processes over the upwind slope. Trajectories calculated using winds from



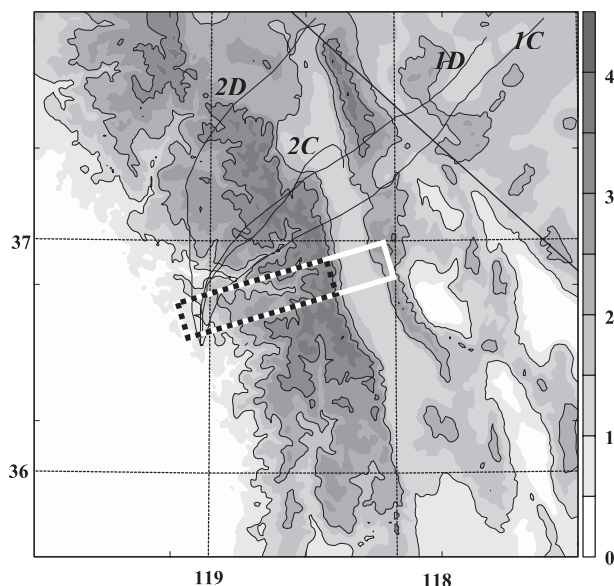


FIG. 12. Two pairs of trajectories are shown, corresponding to parcels launched from a point at the western side of Sierras and from 2500 and 3000 m MSL, computed using the winds from CTRL5 and DRY5, respectively. The symbols C and D in the labels indicate trajectories from CTRL5 and DRY5, and the number 1 and 2 correspond to the parcels from the 3000- and 2500-m level, respectively. The dark-dotted box over the upwind slope indicates the area where the upwind slope blocking index are computed and the larger white box corresponds to the area over which the wave amplification factors are computed.

the IOP-8 simulations confirm the presence of a deep blocked layer to the west of the main Sierra ridge. However, compared to the other three IOPs, the difference between the moist and dry trajectories of IOP-8 is much smaller, likely due to the shallow nature of the moist layer and weak low-level cross-barrier winds in IOP-8.

#### d. The impact of moisture above the mountaintop on waves

To examine the impact of moisture aloft on the mountain-wave amplitude, we define an wave amplification factor,  $\hat{W}(z) = W(z)/W_s$ , where  $W(z) = \sqrt{\rho(z)} \iint_B |w| dx dy$  is a bulk measure of density-weighted wave strength at level  $z$ ,  $W_s$  is  $W$  along the terrain surface, and  $\rho(z)$  is the air density. The symbol  $B$  denotes the area of the rectangular box oriented along the UWKA flight track across the Sierra ridge and Owens Valley (Fig. 12). The wave amplification factors computed from the four pairs of simulations around the observational times are shown in Fig. 14. It is evident that, in the middle troposphere and above, the wave amplification factor from the dry simulation of IOP 5 is significantly larger than from the corresponding control simulation. For example, the ratio of  $\hat{W}(z = 7.5 \text{ km})$

values from DRY5 and CTRL5 is 1.6 (i.e., given the same perturbation source, the wave amplitude in the dry atmosphere could be more than 50% larger than in the corresponding moist atmosphere). Presumably, the relatively deep moist layer in the lower to middle atmosphere during IOP-5 significantly weakens the waves, likely through reduction of the buoyancy force.

For IOP-6c,  $\hat{W}(z)$  derived from DRY6c is larger than that from the corresponding control simulation as well. At  $z = 7.5 \text{ km}$ , the  $\hat{W}(z)$  ratio for DRY6c and CTRL6c is around 1.3, which is substantially smaller than that derived from the IOP-5 simulations, likely because the moist layer is shallower in IOP-6c than in IOP-5. For IOP-8 and IOP-12, in the middle troposphere, the  $\hat{W}(z)$  values from the dry simulations are always larger than from the corresponding control simulations, implying that the moist layer above the mountaintop level tends to weaken mountain waves. The difference between the  $\hat{W}(z)$  profiles from DRY8 and CTRL8 is much smaller than the other three IOPs, which is consistent with the thin liquid clouds over the upwind slope shown in the CTRL8 vertical cross section (Fig. 8). It is noteworthy that the above results are relatively insensitive to the location of the downstream boundary of the box (Fig. 12), as long as the primary waves in the lee of the Sierra ridge (Figs. 6–9) are inside the box. The damping effect of a moist layer adjacent to the topography on mountain waves is consistent with previous studies (e.g., Barcilon et al. 1980; Durran and Klemp 1982a).

In summary, the diagnosis of the four pairs of simulations suggests that moisture modulates mountain waves mainly through two competing processes. Below the mountaintop level, moisture tends to enhance waves through reducing blocking and therefore increasing the effective terrain height. The moist layer immediately above the terrain tends to attenuate waves (referred to as damping effect hereafter). For IOP-5, -6c, and -12, the damping effect dominates and the resultant mountains waves are weaker in the control simulations than in the corresponding dry simulations. For IOP-8, the two mechanisms are likely comparable.

## 5. Discussion

Both low-level flow blocking and microphysical processes are highly nonlinear and analytically intractable. Instead of explicitly dealing with these nonlinear processes, in this section, we attempt to seek a consistent qualitative interpretation of the observed and simulated wave characteristics and their dependence on moist processes using the traditional moist buoyancy frequency concept, the equivalent terrain concept (Smith et al. 2002), a multiple layer linear wave model, and a set of idealized simulations.

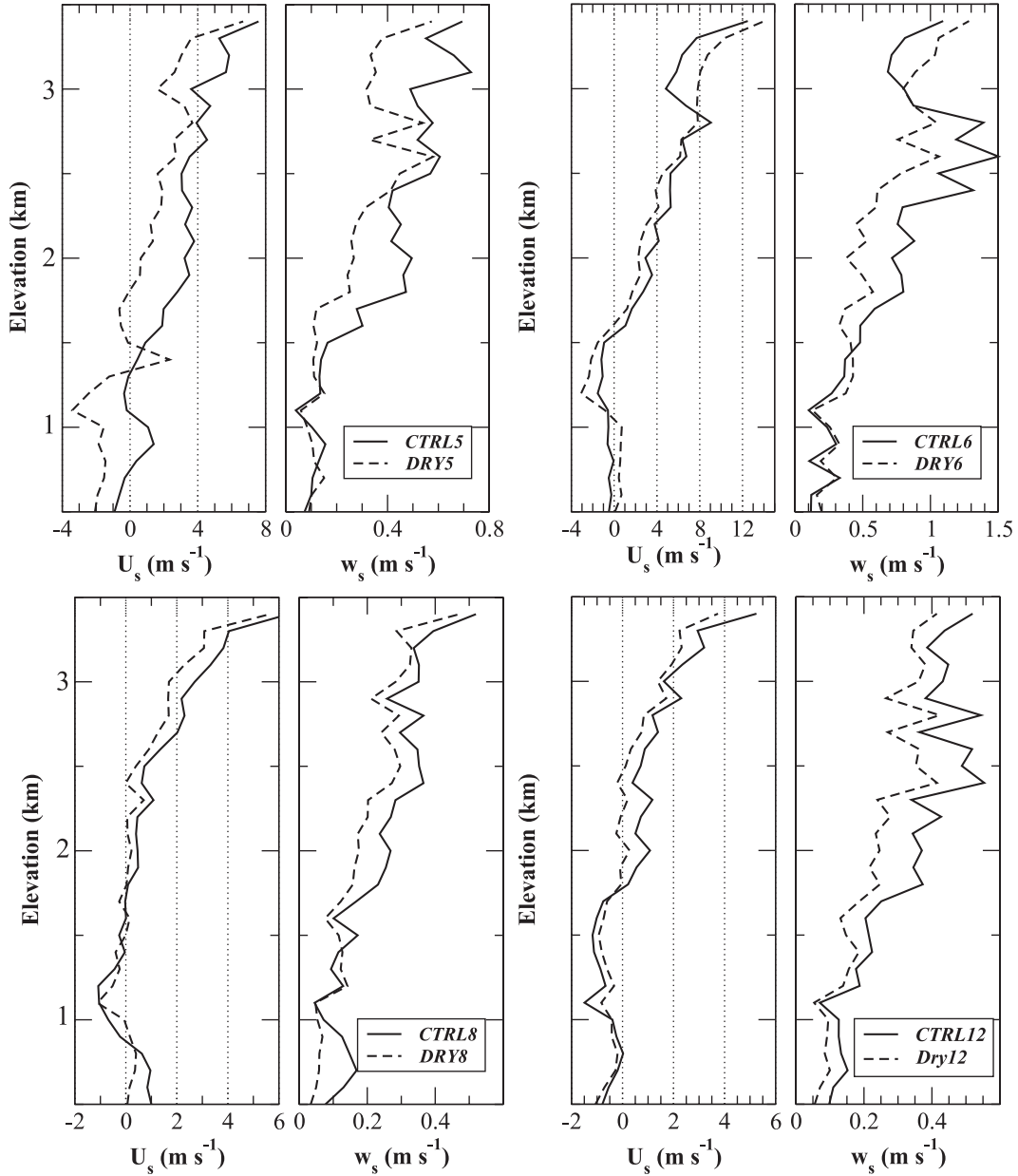


FIG. 13. The average cross-barrier wind component and the vertical velocity over the upwind slope in the dotted box shown in Fig. 12 are plotted against the terrain elevation. They are derived from the four pairs of simulations approximately at the UWKA observational times.

*a. Moist buoyancy frequency and effective mountain height*

As discussed in the introduction, if we assume that the precipitation is weak and the moist processes involved are reversible, the moist buoyancy frequency of a saturated atmosphere can be written as (Durrán and Klemp 1982b)

$$N_w^2 = \frac{g}{T} \left( \frac{dT}{dz} + \Gamma_m \right) \left( 1 + \frac{Lq_s}{RT} \right) - \frac{g}{1 + q_w} \frac{dq_w}{dz}, \quad (3)$$

where

$$\Gamma_m = \Gamma_d (1 + q_w) \left( 1 + \frac{Lq_s}{RT} \right) \left[ 1 + \frac{c_{pv}q_s + c_wq_L}{c_p} + \frac{\varepsilon L^2 q_s}{c_p R T^2} \left( 1 + \frac{q_s}{\varepsilon} \right) \right]^{-1}$$

is the moist adiabatic lapse rate, the symbols  $q_w$ ,  $q_L$ , and  $q_s$  denote the mixing ratios of water vapor, liquid water,

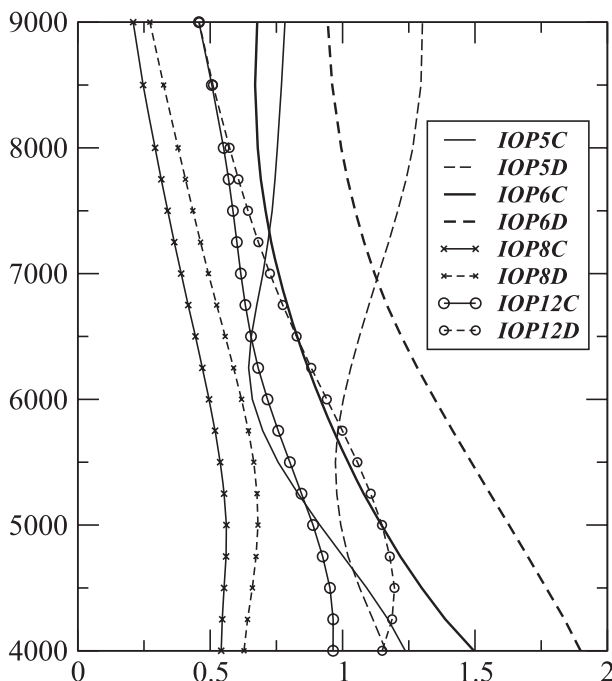


FIG. 14. The wave amplification factors (see text for definition) over the white box in Fig. 12 computed from the four pairs of simulations are shown. They approximately correspond to the UWKA observational times.

and solid water. For the four upstream soundings shown in Fig. 5, the moist buoyancy frequency  $N_w$  is calculated using (3). For  $N_w^2 < 0$  (i.e., the moist layer may be convectively unstable), we let  $N_w = -\sqrt{-N_w^2}$ . When the upstream airflow is unsaturated, Eq. (3) can still be used to calculate  $N_w$  by assuming that the unsaturated air column is lifted to the lifting condensation level (LCL) uniformly. Reeves and Rotunno (2008) have demonstrated that the LCL plays a role in upstream blocking when the upstream air is unsaturated. However, in this study, the RH is approximately 90% in the lower atmosphere and the corresponding LCL is between 100 and 200 m, which is much less than the ridge height ( $\sim 3.5$  km) and the characteristic vertical wavelengths ( $\sim 6$  km).

As expected, in general,  $N_w$  is smaller than  $N$  and the difference decreases with increasing altitude (Fig. 15). For IOP-5 and IOP-12, the layer depth with a substantially smaller  $N_w$  is roughly 6 km due to the deep moist layer in these two IOPs (Fig. 5). It is also noteworthy that  $N_w$  is negative in the lower troposphere for IOP-8, which is consistent with the presence of convective clouds in the GOES images (Fig. 4c).

Smith et al. (2002) has shown that, using the effective terrain height, a linear wave model could reproduce the observed wave characteristics over Mount Blanc (4810 m

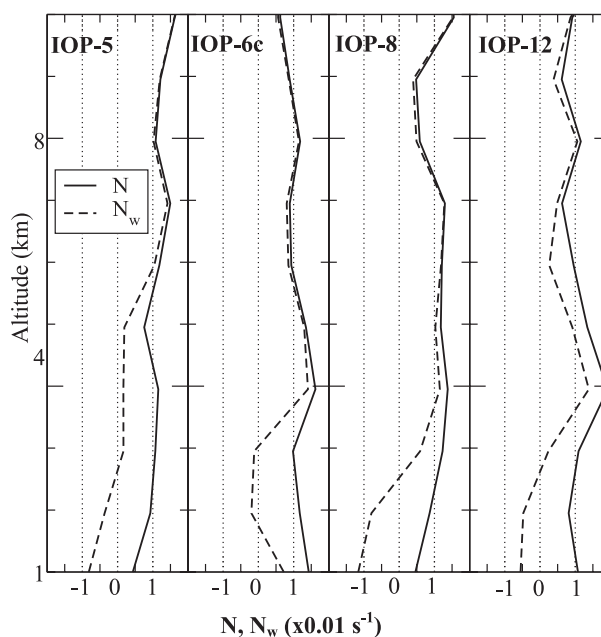


FIG. 15. Moist and dry buoyancy frequency profiles calculated using Eq. (3) for the four upstream soundings shown in Fig. 5.

MSL), the highest peak in the Alps, reasonably well. Based on previous studies, we hypothesize that the effective terrain height is given by

$$\frac{N h_{\text{eff}}}{U_c} = M_c, \quad (4)$$

where  $M_c$  is the critical nondimensional mountain height for the Sierra ridge. The depth of the blocked layer is then given by  $h_{\text{cutoff}} = h_m - h_{\text{eff}}$ , where  $h_m = 3.5$  km is chosen as the mean Sierra ridge crest height.

It is instructive to evaluate how much low-level moisture may have modified the effective terrain height for the four moist cases using (4) and the upstream soundings. It is evident that  $U_c$ ,  $N$ , and  $N_w$  vary strongly with altitude (Figs. 5 and 15). To solve (4) for  $h_{\text{eff}}$ , we first calculate the average  $U_c$ ,  $N$ , and  $N_w$  in each 100-m vertical range bin below 3.5 km MSL. We further hypothesize that if the blocking criterion is met at a certain level, the flow at and below that level is blocked. Hence, the effective terrain height is determined as the minimum  $h_{\text{eff}}$  that satisfies  $h_{\text{eff}} N(z = h_m - h_{\text{eff}}) / U_c(z = h_m - h_{\text{eff}}) > M_c$ . For  $M_c = 1$ , Eq. (4) is solved using the cross-barrier wind component  $U_c$  and the dry and moist  $N$  derived from the four upstream soundings, respectively. The results are included in Table 2.

As expected, a deep blocked layer exists for both IOP-8 and IOP-12, associated with weaker cross-barrier winds below the mountaintop level (Fig. 5). IOP-6c is characterized by the strongest cross-barrier winds and the

TABLE 2. The cutoff terrain heights derived from the upstream radiosondes using Eq. (4) and the moist–dry wave amplitude ratios (see text for definition) derived from the linear model are listed for the four moist IOPs. The corresponding ratios derived from the COAMPS simulations and averaged over 3 h around each flight time are also included for comparison.

IOP	$h_{\text{cutoff}}$ (m) moist	$h_{\text{cutoff}}$ (m) dry	Ratio (linear)	Ratio (COAMPS)	Note
5	2150	2450	0.42	0.40	Moderate low-level winds and deep moist layer
6c	1200	2450	0.75	0.81	Strong low-level winds and shallow moist layer
8	3250	3350	0.85	0.96	Weak low-level winds and shallow moist layer
12	2550	3050	0.82	0.84	Weak low-level winds and deep moist layer

depth of the blocked layer is the smallest accordingly. It is noteworthy that the low-level moisture reduces the blocked layer depth by more than 1 km for IOP-6c, which likely contributes to the large normalized wave amplitude (i.e., close to unity; Fig. 3). For IOP-5 and IOP-12, the presence of low-level moisture causes a moderate reduction (i.e., 300–500 m) in the blocked flow depth. For IOP-8, the blocked flow depth shows little dependence on moisture, implying that the moist layer is largely blocked. The impact of the effective terrain height variation on the mountain-wave amplitude will be further illustrated in the next section using a linear wave model.

#### b. Impact of moisture on linear waves

The linear wave model we use here has been described in Smith et al. (2002) and Doyle and Jiang (2006). After applying fast Fourier transform to the horizontal dimensions, the steady-state linear wave equation is solved in the wavenumber space in each discrete layer characterized by a uniform buoyancy frequency  $N_i$  and horizontal velocity ( $U_i$ ,  $V_i$ ), where  $i$  is the layer index. At the interface of two adjacent layers, matching conditions are applied to ensure the continuity of mass and pressure. A linearized impermeable boundary condition,  $w(0) = \mathbf{V}_1 \cdot \nabla h$ , is employed along the ground surface, where  $\mathbf{V}_1$  is the wind vector in the first layer and  $\nabla h$  is the terrain slope. In the top layer, a radiation boundary condition is applied which only retains the outgoing waves. Finally, the wave solution in the physical space is derived using the inverse fast Fourier transform.

As discussed in the previous sections, to apply a linear wave model to the problem of moist airflow past high topography such as the Sierra Mountains, the nonlinear processes, low-level flow blocking and the adiabatic warming or cooling associated with microphysical processes, need to be properly represented. In this study, these two processes are represented by the moist buoyancy frequency and the cutoff terrain height (Table 2), respectively. The cutoff terrain height method has been successfully applied to the Alpine waves in the presence

of a deep blocked layer by Smith et al. (2002). The moist buoyancy frequency is a rather crude representation of microphysical processes. Nevertheless, the incorporation of a cutoff mountain height and moist  $N$  into a linear model provides the simplest theoretical framework for qualitatively evaluating the relative importance of the two competing moisture effects on mountain waves.

The wave amplitude ratios derived from the corresponding moist and dry pairs of linear solutions are included in Table 2. The model includes fifteen 1-km-thick layers with a radiation boundary condition applied at  $z = 15$  km. The model domain, centered at Independence is composed of 1024 by 1024 grid points with a grid spacing of 2 km. Periodic conditions are applied along the sidewalls. For each case, the moist (dry) wave solutions are obtained using the moist (dry)  $h_{\text{cutoff}}$  and moist (dry)  $N$ , respectively. Again, the wave amplitude is defined as the maximum  $w$  range in the UWKA vertical cross section between the mountaintop level and 8 km MSL.

According to Table 2, although the effective terrain height for IOP-5 is 300 m higher in the presence of moist processes, the moist wave amplitude is substantially reduced, implying that the destratification mechanism dominates. The derived moist–dry wave amplitude ratio is comparable to the observations (Fig. 3b) and the COAMPS simulations. Note that the ratios derived from COAMPS simulations are averaged over 3 h around each UWKA flight period. For IOP-6c, the effective terrain height is significantly higher with moisture and yet the waves are still stronger in the dry solution. The moist–dry wave amplitude ratios from the linear model and from COAMPS are comparable and are slightly less than unity, implying that the two competing mechanisms for moisture to modulate waves largely offset each other for IOP-6c. Moist processes have the least influence on waves during IOP-8. The thin moist layer is mostly blocked to the upwind side of the Sierra ridge and the impact of moist processes on low-level flow blocking and destratification aloft is insignificant. For IOP-12, moisture reduces the blocked flow depth by 500 m and the moist wave is approximately 20% weaker than the corresponding dry wave, indicating that the damping effect dominates as in IOP-5. Compared to IOP-5, the

moist–dry wave amplitude ratio is much larger for IOP-12, likely due to its thinner moist layer.

*c. Sensitivity of wave amplitudes to upstream moist layer depth*

Both the diagnosis of nonlinear numerical solutions and linear analysis consistently indicate the two competing effects of moist processes on mountain waves: reducing blocking and damping effects. To further confirm the sensitivity of wave amplitudes to the upstream moist layer depth, a set of idealized simulations of homogeneous flows past a finite ridge have been carried out. The computational domain comprises  $201 \times 201$  grid points with a horizontal grid spacing of 5 km. There are 60 vertical levels, identical to those real-data simulations, with the exception that a radiation condition is applied at the model top to reduce downward wave reflection. A bell-shaped ridge is located at the center of the domain, given by

$$h(x, y) = h_m (1 + x^2/a^2 + y^2/b^2)^{-3/2}, \quad (5)$$

where  $h_m = 4500$  m is the ridge crest height,  $a = 40$  km and  $b = 200$  km are the ridge half-width and length, respectively. The model is initialized using a single sounding from IOP-5 or IOP-6c (Fig. 5). For each case, three simulations have been carried out with the original RH profile (referred to as RHCTRL), reduced RH from above (i.e., RH in the top 0.5 km of the moist layer is reduced to 50%, referred to as RHRA), and reduced RH from below (i.e., RH in the lowest 0.5 km of the moist layer is reduced to 50%, referred to as RHRB), respectively. The incoming flow is steady and in geostrophic balance and the model is integrated over 12 h.

The RHCTRL simulations using the IOP-5 and -6c soundings are characterized by trapped wave and hydrostatic waves, respectively, qualitatively similar to the corresponding real-data simulations. For both cases, the RHRA runs produce substantially stronger waves than the corresponding RHCTRL runs, implying that a deeper moist layer tends to damp the wave amplitude more. As expected, compared to the RHCTRL run, the cross-ridge wind component and vertical velocity over the upwind slope are notably reduced in the RHRB run of IOP-6c, indicative of more severe blocking due to the drier low-level flows. Consequently, the wave amplitude is substantially smaller in the RHRB run. For IOP-5, both the surface winds over the upwind slope and the wave aloft are weaker in the RHRB run as well. However, the differences between the RHCTRL and the RHRB runs are small.

In summary, these idealized simulations are consistent with the notion that moist processes modulate

mountain waves through two competing mechanisms: reducing low-level blocking and damping waves.

## 6. Conclusions

Analysis of the aircraft measurements of mountain waves and the cross-barrier wind profiles from upstream radiosondes obtained during T-REX suggests that the mountain-wave amplitude linearly increases with the upstream cross-barrier wind component at the mountaintop level and moisture in general tends to weaken mountain waves. For some very moist cases, the observed wave amplitude was less than one-third of the reference wave amplitude derived from the UWKA measurements obtained during the 2-month-long T-REX period.

Motivated by these observations, four moist cases documented during the T-REX have been examined using a mesoscale model with explicit cloud parameterizations and a linear wave model to understand the role of moisture in modulating mountain waves. Two competing mechanisms have been identified by contrasting a control and corresponding dry simulations of four moist cases, and are schematically summarized in Fig. 16. Latent heat release associated with condensation over the upwind slope of topography tends to enhance the ascent of airflow over high terrain and therefore reduce the upwind flow blocking. This result is consistent with the idealized study of moist stratified flow past an isolated mountain by Jiang (2003). In contrast, a moist layer adjacent to the terrain surface tends to damp waves through reducing the buoyancy frequency. This effect can be qualitatively described using the moist buoyancy frequency concept and reproduced by a linear wave model. Recently, Jiang and Doyle (2008) demonstrated that a neutrally stratified layer over a terrain surface could substantially reduce mountain-wave drag. Our results are in general consistent with these findings.

The relative importance of the two competing processes is determined by the moisture and cross-barrier wind profiles, as well as the mountain height. With moderate or strong cross-barrier winds below the mountaintop level and a deep moist layer extending from the surface to the middle troposphere (i.e., IOP-5 and Fig. 16a), the depth of the blocked layer could be substantially reduced by moist processes, and accordingly, the equivalent terrain height is increased. Likewise, the deep moist layer also reduces the stratification in the lower to middle troposphere and weakens waves. Overall, the damping effect of moisture dominates and mountain-wave amplitudes could be significantly weakened by the deep moist layer. With strong low-level cross-barrier



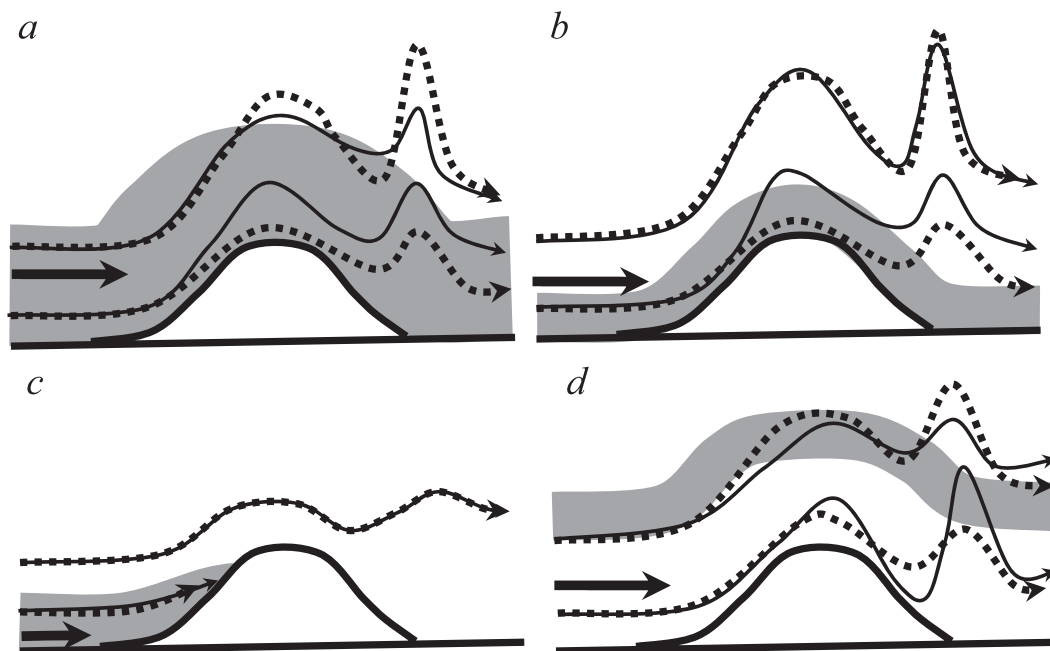


FIG. 16. Schematic plots of mountain-wave response to locations and depths of the moist layer: (a) deep moisture layer and strong low-level winds, (b) shallow moisture layer and strong low-level winds, (c) shallow moisture layer and weak low-level winds, and (d) moisture layer over a dry layer. The solid and dashed curves correspond to the moist and dry streamlines, respectively. The shaded areas indicate the locations and depths of the moist layer. The bold arrows indicate the cross-ridge wind component; the longer the arrow, the stronger the winds.

winds and a relatively shallow moist layer over the surface (i.e., IOP-6c and Fig. 16b), the two competing moist effects, reducing blocking and damping, could largely offset each other and the overall influence of moisture on the wave amplitude is relatively small. Consequently the moist–dry wave amplitude ratio is relatively large (i.e., close to unity). When the moist layer is mostly confined below the mountaintop level where the cross-barrier winds are weak (e.g., IOP-8 and Fig. 16c), the moist layer could be largely blocked by the high Sierra ridge. Consequently, the latent heat release associated with the upslope ascent or wave-induced vertical motion aloft is relatively small, and the influence of moisture on mountain waves is insignificant. IOP-12 is qualitatively similar to IOP-5 except that the cross-barrier winds are weaker. Accordingly, the blocked layer is deeper and the waves are weaker. As shown in Fig. 16d, the moist layer above a dry layer could serve as a waveguide, which damps waves in and above the moist layer (Durran and Klemp 1982a) and enhances waves in the dry layer below (Barcilon et al. 1980; Doyle and Smith 2003). However, this scenario was not observed during T-REX. Given the potential impact of moisture on mountain waves identified in this study, further exploration of the complex relationship between moisture and flow over topography is required. Proper repre-

sentation of those moist processes will be needed in next-generation gravity wave drag and flow blocking parameterization for large-scale models.

**Acknowledgments.** This research was supported by the Office of Naval Research (ONR) Program Element 0601153 N. The first author was partially funded by National Science Foundation (Grant ATM-0749011). The simulations were made using the Coupled Ocean–Atmosphere Mesoscale Prediction System (COAMPS) developed by the U.S. Naval Research Laboratory.

## REFERENCES

- Barcilon, A., and D. Fitzjarrald, 1985: A nonlinear steady model for moist hydrostatic mountain waves. *J. Atmos. Sci.*, **42**, 58–67.
- , J. C. Jusem, and P. G. Drazin, 1979: On the two-dimensional hydrostatic flow of a stream of moist air over a mountain ridge. *Geophys. Astrophys. Fluid Dyn.*, **13**, 125–140.
- , —, and S. Blumsack, 1980: Pseudo-adiabatic flow over a two dimensional ridge. *Geophys. Astrophys. Fluid Dyn.*, **16**, 19–33.
- Buzzi, A., N. Tartaglione, and P. Malguzzi, 1998: Numerical simulations of the 1994 Piedmont flood: Role of orography and moist processes. *Mon. Wea. Rev.*, **126**, 2369–2383.
- Colle, B. A., 2004: Sensitivity of orographic precipitation to changing ambient conditions and terrain geometries: An idealized modeling perspective. *J. Atmos. Sci.*, **61**, 588–606.

- , Y. Lin, S. Medina, and B. F. Smull, 2008: Orographic modification of convection and flow kinematics by the Oregon Coast Range and Cascades during IMPROVE-2. *Mon. Wea. Rev.*, **136**, 3894–3916.
- Cox, J. A. W., W. J. Steenburgh, and J. C. Shafer, 2005: The kinematic structure of a Wasatch Mountain winter storm during IPEX IOP3. *Mon. Wea. Rev.*, **133**, 521–542.
- Doyle, J. D., and R. B. Smith, 2003: Mountain waves over the Hohe Tauern. *Quart. J. Roy. Meteor. Soc.*, **129**, 799–823.
- , and Q. Jiang, 2006: Observations and numerical simulations of mountain waves in the presence of directional wind shear. *Quart. J. Roy. Meteor. Soc.*, **132**, 1877–1905.
- Durran, D. R., and J. B. Klemp, 1982a: The effects of moisture on trapped mountain lee waves. *J. Atmos. Sci.*, **39**, 2490–2506.
- , and —, 1982b: On the effects of moisture on the Brunt–Väisälä frequency. *J. Atmos. Sci.*, **39**, 2152–2158.
- , and —, 1983: A compressible model for the simulation of moist mountain waves. *Mon. Wea. Rev.*, **111**, 2341–2361.
- Grubišić, V., and Coauthors, 2008: The Terrain-Induced Rotor Experiment: An overview of the field campaign and some highlights of special observations. *Bull. Amer. Meteor. Soc.*, **89**, 1513–1533.
- Harshvardhan, R. Davies, D. Randall, and T. Corsetti, 1987: A fast radiation parameterization for atmospheric circulation models. *J. Geophys. Res.*, **92**, 1009–1015.
- Hodur, R. M., 1997: The Naval Research Laboratory's Coupled Ocean/Atmospheric Mesoscale Prediction System (COAMPS). *Mon. Wea. Rev.*, **125**, 1414–1430.
- Huppert, H. E., and J. W. Miles, 1969: Lee waves in a stratified flow. Part 3: Semi-elliptical obstacles. *J. Fluid Mech.*, **35**, 481–496.
- Jiang, Q., 2003: Moist dynamics and orographic precipitation. *Tellus*, **55A**, 301–316.
- , and J. D. Doyle, 2008: On the diurnal variation of mountain waves. *J. Atmos. Sci.*, **65**, 1360–1377.
- Kain, J. S., and J. M. Fritsch, 1993: Convective parameterization for mesoscale models: The Kain–Fritsch scheme. *The Representation of Cumulus Convection in Numerical Models, Meteor. Monogr.*, No. 46, Amer. Meteor. Soc., 165–170.
- Klemp, J. B., and D. K. Lilly, 1978: Numerical simulation of hydrostatic mountain waves. *J. Atmos. Sci.*, **35**, 78–107.
- Louis, J. F., 1979: A parametric model of vertical eddy fluxes in the atmosphere. *Bound.-Layer Meteor.*, **17**, 187–202.
- , M. Tiedtke, and J. F. Geleyn, 1982: A short history of the operational PBL-parameterization at ECMWF. *Proc. Workshop on Planetary Boundary Layer Parameterization*, Reading, United Kingdom, European Centre for Medium-Range Weather Forecasts, 59–79.
- Mellor, G. L., and T. Yamada, 1974: A hierarchy of turbulence closure models for planetary boundary layers. *J. Atmos. Sci.*, **31**, 1791–1806.
- Miglietta, M. M., and A. Buzzi, 2001: A numerical study of moist stratified flows over isolated topography. *Tellus*, **53A**, 481–499.
- , and R. Rotunno, 2005: Simulations of moist nearly neutral flow over a ridge. *J. Atmos. Sci.*, **62**, 1410–1427.
- Reeves, H. D., and R. Rotunno, 2008: Orographic flow response to variations in upstream humidity. *J. Atmos. Sci.*, **65**, 3557–3570.
- Rutledge, S. A., and P. V. Hobbs, 1983: The mesoscale and microscale structure of organization of clouds and precipitation in midlatitude cyclones. VIII: A model for the “seeder-feeder” process in warm-frontal rainbands. *J. Atmos. Sci.*, **40**, 1185–1206.
- Scorer, R. S., 1949: Theory of lee waves of mountains. *Quart. J. Roy. Meteor. Soc.*, **75**, 41–56.
- Smith, R. B., 1989: Mountain-induced stagnation points in hydrostatic flow. *Tellus*, **41A**, 270–275.
- , and Y. L. Lin, 1982: The addition of heat to a stratified airstream with application to the dynamics of orographic rain. *Quart. J. Roy. Meteor. Soc.*, **108**, 353–378.
- , and S. Grønås, 1993: Stagnation points and bifurcation in 3-D mountain airflow. *Tellus*, **45A**, 28–43.
- , S. T. Skubis, J. D. Doyle, A. Broad, C. Kiemle, and H. Volkert, 2002: Mountain waves over Mt. Blanc: Influence of stagnant boundary layer. *J. Atmos. Sci.*, **59**, 2073–2092.
- , B. K. Woods, J. Jensen, W. A. Cooper, J. D. Doyle, Q. Jiang, and V. Grubišić, 2008: Mountain waves entering the stratosphere. *J. Atmos. Sci.*, **65**, 2543–2562.